1. Experimental Details

Resonant Inelastic X-ray Scattering (RIXS) measurements were performed at the ID32 beamline of the European Synchrotron Radiation Facility (ESRF) with energy resolution of 60 meV, as determined from the full-width at half-maximum (FWHM) of the non-resonant spectrum of a standard polycrystalline silver sample. The Hg1201 single crystal was cleaved *ex situ* prior to the RIXS measurements. The hole concentration was estimated from the T_c vs p relationship established in Ref. [S1]. Fig. S1(a) shows a schematic of the scattering geometry. Momentum scans were performed by rotating the sample about the **b** axis with the detector angle fixed at $2\theta = 150°$. We obtained energy-momentum intensity maps along $[H,0]$ for the H values indicated in Fig. S1(b). At each momentum transfer, we measured the excitation spectrum for approximately 45 minutes. Additionally, X-ray absorption spectra were periodically taken to ensure that the incident X-ray energy remained at the maximum of the Cu L_3 resonance edge. Raw data are shown in Fig. S2.

At each momentum transfer, the energy zero was determined by measuring the non-resonant spectrum of a polycrystalline silver standard located near the sample. The data were collected in short time intervals of 45 min, and each scan was corrected for the energy shift, if any was observed. In order to avoid errors in the determination of the energy zero, the thickness of the silver was approximately the same as the thickness of the sample, and both were placed on the same axis of rotation. As a consistency check, we monitored the energy of *d-d* excitations and found no significant change with temperature in the effective *d-d* excitation energy, and hence in the energy zero (see Fig. S2). Importantly, the energy resolution (60 meV, FWHM) and observed energy scales (~40 meV and ~165 meV) are large compared to typical beamline energy drifts, thus minimizing the chance of an adverse affect on our conclusions.

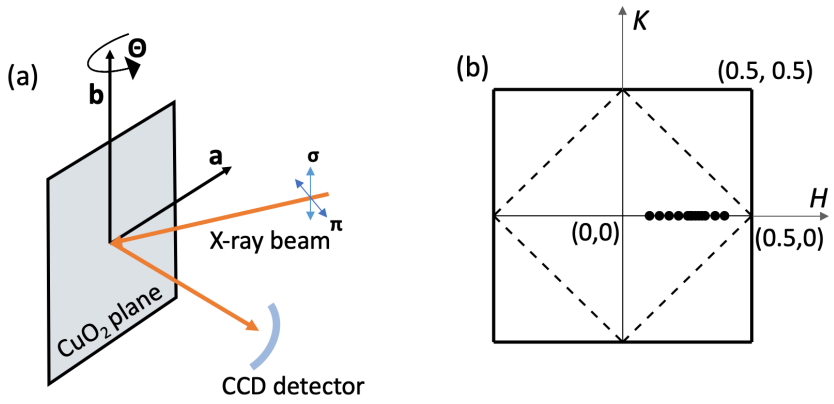


Fig. S1. (a) Scattering geometry with two different incident photon polarizations: parallel (π) and perpendicular (σ) to the $(H,0,L)$ scattering plane. (b) Reciprocal-space schematic with first nuclear and antiferromagnetic Brillouin zones (solid and dashed lines, respectively). Circles: H values accessed in the experiment.

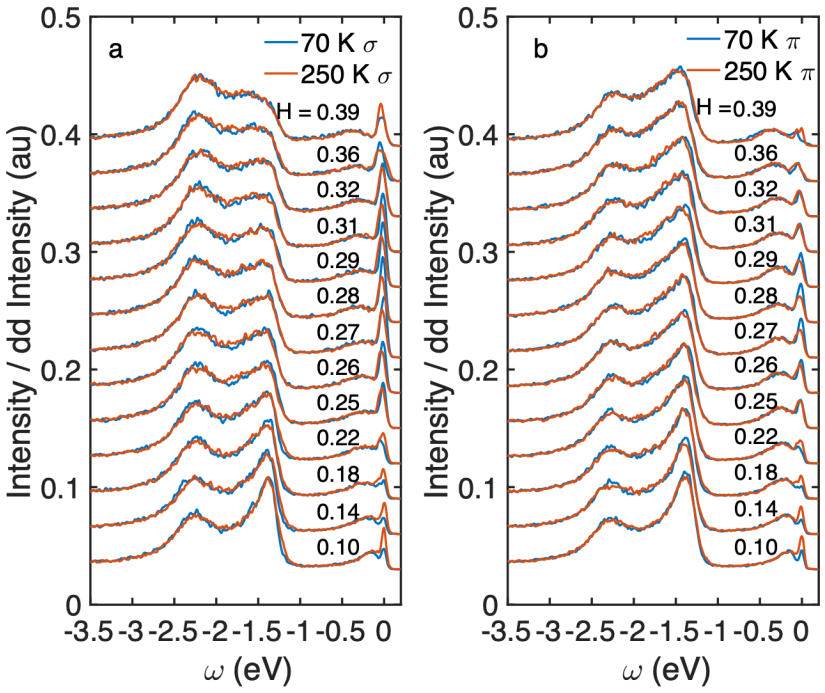


Fig. S2. RIXS spectra measured at 70 K and 250 K with (a) σ- and (b) π-polarized incident photons. Since the intensity of *d*-*d* excitations (between -1 and -3 eV) is nearly temperature independent, its lower energy slope serves as a good indicator of the correct energy calibration.

2. Paramagnons

In order to extract the paramagnon response, we decompose the mid-infrared region of the RIXS spectra into three components (Fig. S3) using the heuristic formula [S2, S3]:

$$\frac{I}{I_{dd}}(\omega) = G(\omega) + n_B L(\omega) + n_B \chi''(\omega),$$

where $n_B = [1 - \exp(-\hbar\omega/k_B T)]^{-1}$ is the Bose factor, $G(\omega)$ a resolution-limited Gaussian function that captures the elastic peak, $L(\omega)$ a resolution-limited Lorentzian profile used to effectively capture the phonon contribution, and the paramagnon was fitted to a damped harmonic oscillator form,

$$\chi''(\omega) = \chi_0'' \frac{\gamma\omega}{[\omega^2-\omega_0^2]^2+\omega^2\gamma^2} = \frac{\chi_0''}{2\omega_1}\left[\frac{\gamma/2}{(\omega-\omega_1)^2+(\gamma/2)^2} - \frac{\gamma/2}{(\omega+\omega_1)^2+(\gamma/2)^2}\right],$$

with damping coefficient $\frac{\gamma}{2} = \sqrt{\omega_0^2 - \omega_1^2}$. In addition, a linear background is assumed. In order to model the RIXS spectra, $G(\omega)$, $L(\omega)$ and $\chi''(\omega)$ are further convoluted with the instrument resolution function. The extracted damping coefficient shows no discernible momentum and temperature dependence (Fig. S4).

Figure S4 also compares the magnetic dispersion along [*H*,0] with results for doped and undoped $La_{2-x}Sr_xCuO_4$. The paramagnon dispersions for LSCO ($p = x = 0.11$) [S4] and Hg1201 ($p \approx 0.086$) agree within error up to at least $H = 0.35$ rlu.

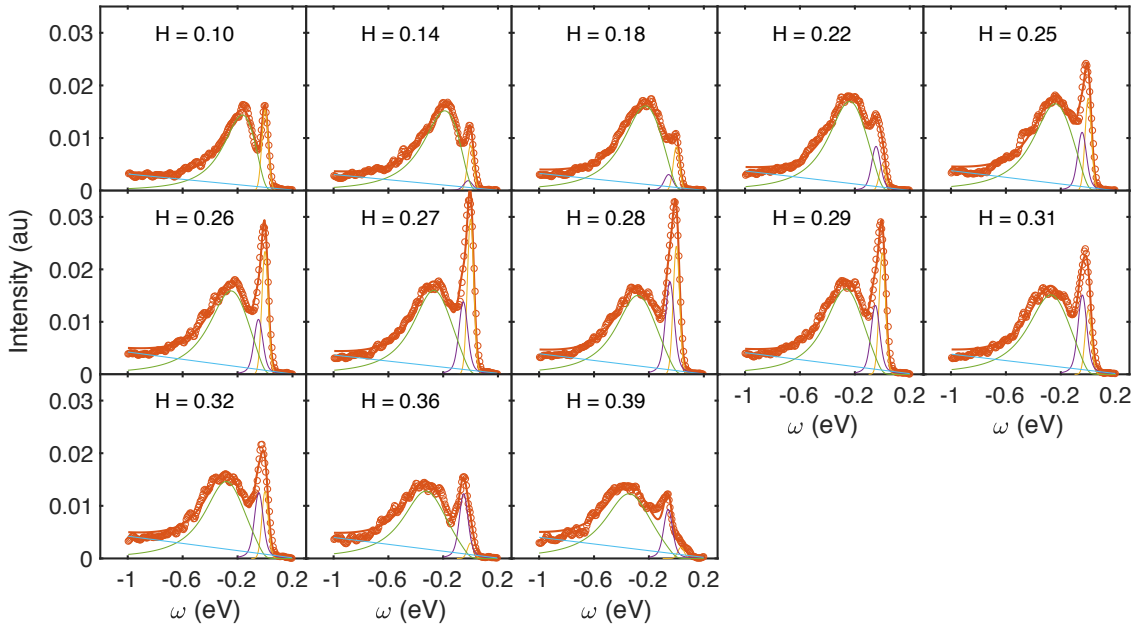


Fig. S3. Fits to RIXS data taken at 70 K in π geometry, in which the paramagnon response is strongest, with in-plane momentum transfer H indicated. The spectra are decomposed into three components plus a linear background (blue): a resolution-limited elastic peak (yellow), a resolution-limited effective phonon peak (purple), and a damped paramagnon excitation (green).

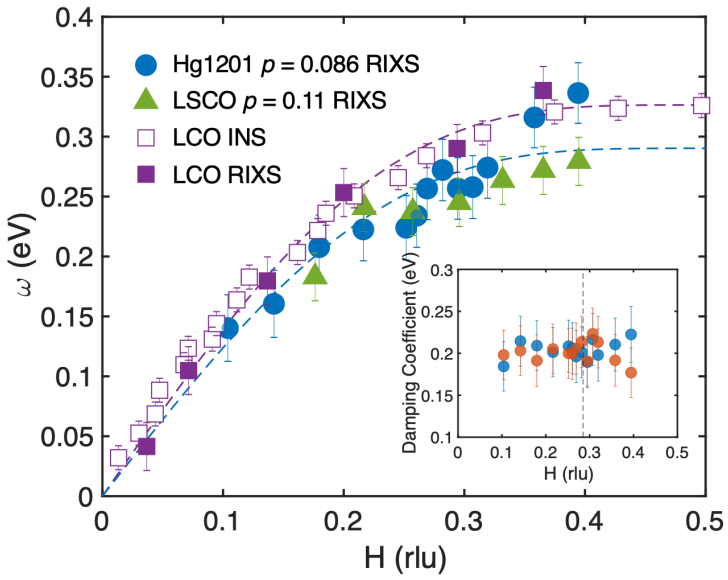


Fig. S4. Dispersion of magnetic excitations in Hg1201 ($p \approx 0.086$) at T = 70 K, compared with undoped antiferromagnetic La_2CuO_4 (LCO) [S2, S5, S6] and 11% Sr-doped $La_{2-x}Sr_xCuO_4$ (LSCO) [S4]. Blue and purple dashed lines are simple heuristic fits to nearest-neighbor spin-wave theory for Hg1201 and LCO, respectively. Inset: Damping coefficient for Hg1201 at 70 K and 250 K, with error bars set to the energy resolution (30 meV, half of the FWHM energy resolution). Neither the paramagnon dispersion nor the damping coefficient shows anomalous behavior at $\mathbf{q}_{CDW}$.

3. Polarization dependence

The Cu L_3-edge RIXS cross section can be calculated using the approximation of isolated Cu^{2+} ions in a tetragonal crystal field with D_{4h} symmetry. Following ref. [S7], we calculate the scattering amplitude for the present experimental geometry. For spin-conserving scattering,

$$F_{\sigma\sigma'} \propto \frac{1}{3}$$

$$F_{\pi\pi'} \propto -\frac{1}{3}\sin\left(\frac{tth}{2}-\delta\right)\sin\left(\frac{tth}{2}+\delta\right)$$

and for spin-flip scattering,

$$F_{\sigma\pi'} \propto -\frac{i}{6}\sin\left(\frac{tth}{2}-\delta\right)$$

$$F_{\pi\sigma'} \propto -\frac{i}{6}\sin\left(\frac{tth}{2}+\delta\right)$$

where σ/π and σ'/π' denote the incident and scattered photon polarization. The angles *tth* and δ are the scattering angle and the rotation angle of the sample from the specular condition ($i.e., \delta = \theta - \frac{tth}{2}$), respectively. By comparing the intensity ratio of two different incident photon polarizations, I_σ/I_π, we can determine the charge or magnetic nature of the excitation. Figure S5 shows the theoretical and experimental polarization dependences in the quasielastic and paramagnon energy range. The comparison demonstrates the respective dominant charge and magnetic origin of the response. We note that this analysis points to the possibility that at both 70 K and 250 K up to 20% of the response in the paramagnon range is due to charge scattering.

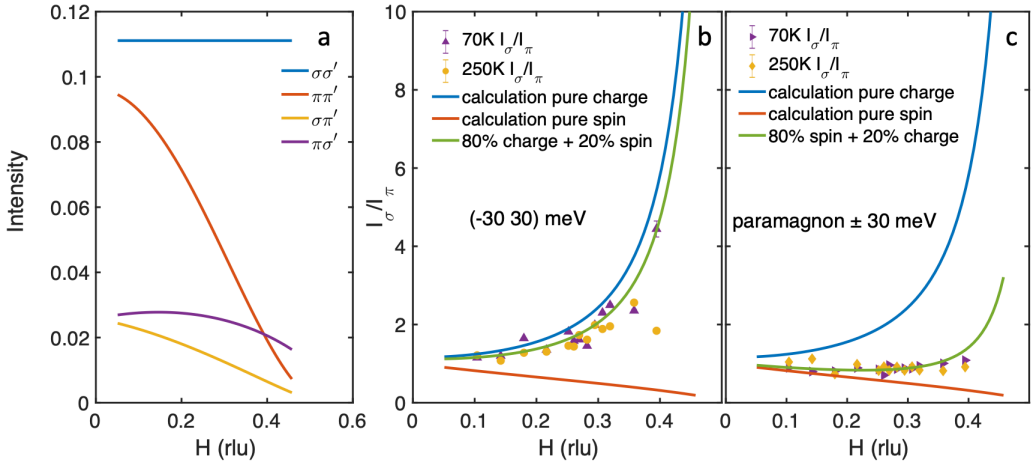


Fig. S5. (a) RIXS intensity calculation assuming isolated Cu^{2+} ions in different scattering geometries. (b) Intensity ratio I_σ/I_π in the quasielastic energy range. (c) Intensity ratio I_σ/I_π in the paramagnon range. Yellow and purple circles: data. Solid lines: calculation.

4. Comparison with $Nd_2Ba_3CuO_{7-\delta}$

Figure S6 compares our result for Hg1201 (Fig. 3a) with data for $NdBa_2Cu_3O_{7-\delta}$ (NBCO) [S8]. In contrast to our data analysis for Hg1201 (Figs. 2 and 3), which removes featureless phonon contributions from the *H*-dependent intensity at/near $\mathbf{q}_{CDW}$, the NBCO data were analyzed under the assumption that phonon contributions at $\mathbf{q} = (H,0)$ can be removed by subtracting data at the same $|\mathbf{q}|$ along $\mathbf{q} = (H,H)$. Although the UD60 (T_c = 60 K) sample studied in ref. [S8] has a doping level that is closer to our Hg1201 (T_c = 70 K) sample, we consider here the phonon-subtracted NBCO data, which are only available for the optimally-doped sample NBCO OP90 (T_c = 90 K) [S8]. The data in Fig. S6 are scaled to match the low-temperature amplitudes. We observe that the relative strengths of the signal at T_c and 250 K is very similar in both cases. Both compounds show quasielastic CDW correlations at T_c. The data analysis of ref. [S8] involved theoretical considerations of nearly critical CDW correlations. At 250 K and 150 K, the characteristic energy of dynamic charge correlations for NCCO OP90 was estimated to be 15 meV, whereas at T_c a value of 7 meV was obtained [S8]. In Fig. S6, we show that the NBCO OP90 data at 250 K can also be modeled as single-mode Stokes and anti-Stokes excitations with energy 18(3) meV, consistent with the result in ref. [S8].

However, as noted, the analysis of NBCO [S8] involved the subtraction of RIXS spectra along [*H*,*H*] from the data of interest along [*H*,0]. We note that phonon scattering along [*H*,*H*] and [*H*,0] is not necessarily equivalent, that the required sample rotation might introduce systematic errors, and that elastic diffuse scattering from the sample surface may have an effective momentum and temperature dependence. In Fig. S7, we fit the phonon-subtracted RIXS spectra for NBCO OP90 to the sum of a Gaussian quasielastic peak (to effectively capture the quasistatic CDW response, a possible net low-energy phonon contribution, and spurious elastic diffuse scattering) and a Gaussian excitation profile with Stokes and anti-Stokes components (to capture a dynamic mode, convoluted with the Gaussian energy resolution). The data at 90 K, 150 K and 250 K are *simultaneously* fit, with the same excitation energy (ω_0), width (γ_0), and amplitude (A_0, further corrected by the thermal Bose factor). In case that the phonon subtraction is incomplete, or of a possible coupling between low-energy phonons and the quasistatic CDW correlations, we allow the width of quasielastic peak (γ_{el}) to be slightly larger than the energy resolution (40 meV, FWHM). We allow the amplitudes of the elastic peaks (A_{el}) to vary at different temperatures to capture the onset of quasistatic CDW correlations. Given the sources of systematic errors noted above, the fits give a good description of the NBCO OP90 data, as seen from Fig. S7. This analysis yields a dynamic charge excitation scale of ω_0 = 38(4) meV, consistent with our result for the lower of the two dynamic energy scales in Hg1201, and it points to an onset of quasistatic CDW correlations between 150 K and 250 K in NBCO OP90.

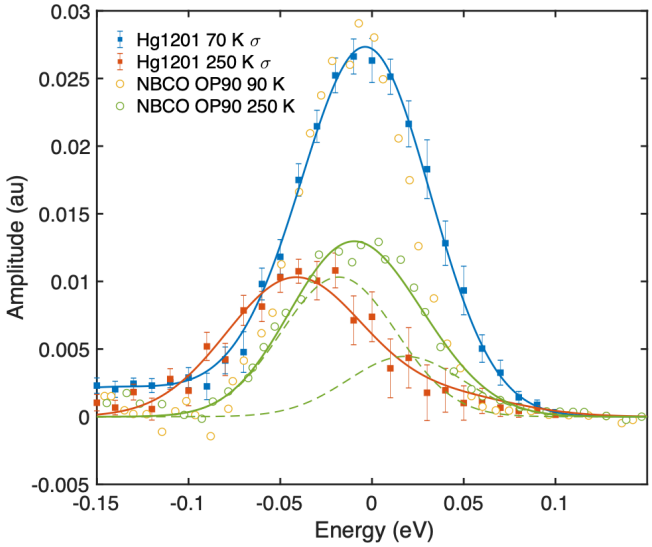


Fig. S6. Comparison of the scattering amplitude for optimally-doped NBCO OP90 (T_c = 90 K) at **q** = (0.31,0), with data obtained at **q** = (0.22,0.22) subtracted [S8] (yellow and green circles), with the present result (Fig. 3a) for Hg1201 (T_c = 70 K; blue and red squares). The solid green line is a heuristic fit to the NBCO OP90 250 K data assuming single-mode Stokes and anti-Stokes contributions (dashed lines). The peak is centered at 18(3) meV, consistent with the analysis result of 15 meV in ref. [S8].

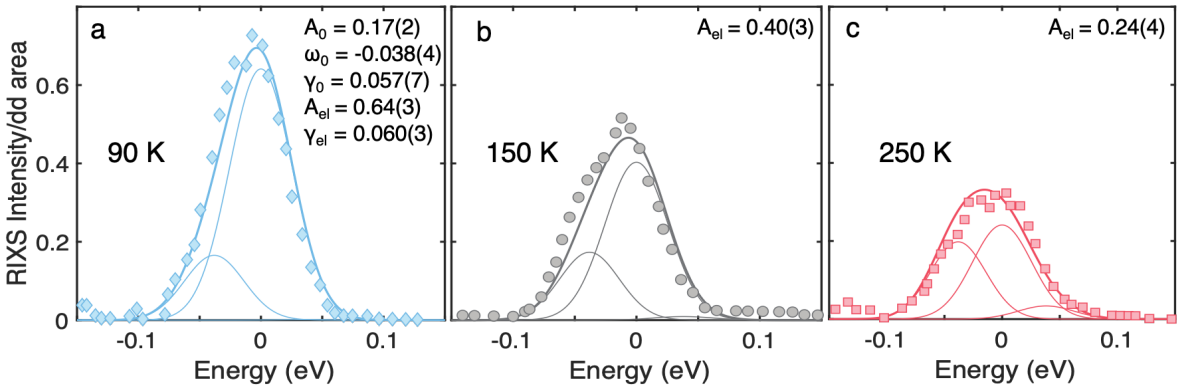


Fig. S7. Analysis of phonon-subtracted NBCO OP90 RIXS data as described in the supplementary text. The solid lines are fits to an effective Gaussian quasielastic peak plus an effective Gaussian excitation profile with Stokes and anti-Stokes components. As seen from the figure, the latter is only relevant at 250 K. No resolution-deconvolution is attempted. Except for the amplitude of the effective quasielastic peak (A_{el}), all parameters are globally fit, i.e., they are the same at all three temperatures. A_0, ω_0 and γ_0 are the amplitude (corrected by the thermal Bose factor), characteristic energy, and FWHM of the dynamic charge mode; γ_{el} is the FWHM of the effective quasielastic peak. The data are reasonably well described with a temperature-independent (up to the thermal Bose factor) dynamic charge response at all temperatures. This analysis yields ω_0 = 38(4) meV and an intrinsic width of 41(10) meV, consistent with the present work for Hg1201.

5. Fit to Log-normal distribution

The analysis in Fig. 3 assumed a single mode at 250 K around 40 meV. The sum of Stokes and anti-Stokes contributions fits well to the data. As noted in the main text, the dynamic charge response can be equally well modeled as a distribution of modes of different energies. We show such an analysis in Fig. S8, where a Log-normal distribution is assumed at zero temperature. Unlike the fit to the heuristic Gaussian form in Fig. 3, which yielded a large intrinsic width, the log-normal distribution is zero in the $\omega = 0$ limit. The high-temperature (250 K) data can be modeled using Bose-Einstein statistics and detailed balance. The lineshape is further convoluted with the Gaussian resolution function. The log-normal distribution extracted from this analysis is used in Fig. 6.

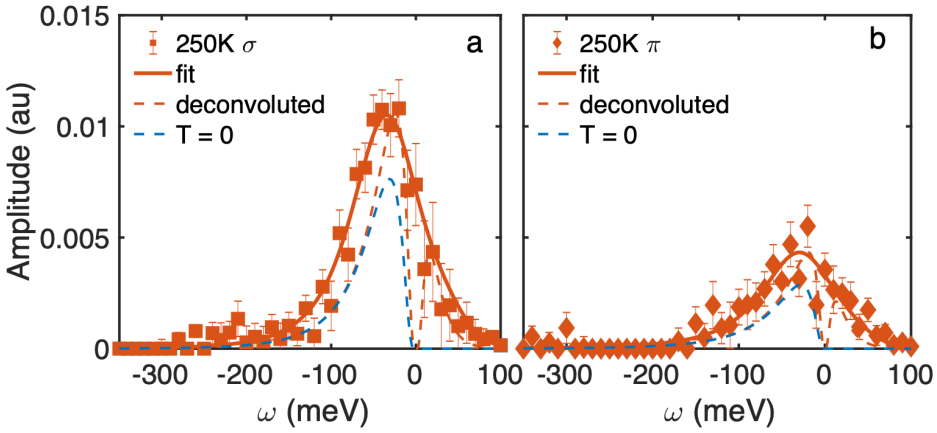


Fig. S8. Hg1201 250 K charge response modeled by a log-normal distribution in (a) σ- and (b) π-polarization. The experimental result (filled square and diamond symbols) is the same as in Fig. 3(a, b). The solid red lines are the results of fits to a resolution-convoluted log-normal distribution with a mean energy of 49(2) meV. The dashed red lines indicate the deconvoluted charge response at 250 K. The blue dashes line is the Bose-corrected charge susceptibility at zero temperature.

6. EI-RIXS

Figure S9 shows RIXS data integrated over various energy ranges. The (-0.2,0.15) eV result corresponds to the range chosen in ref. [S8] and reveals a missing high-energy contribution (Fig. S9c,d). Charge correlations are relevant below ~350 meV (Fig. S9e,f,), consistent with Figs. 2 and 3.

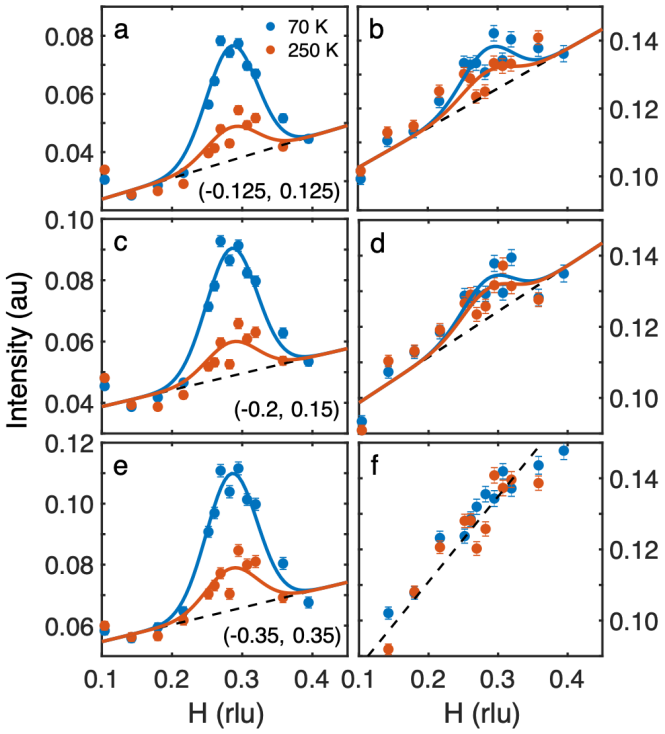


Fig. S9. RIXS spectra integrated over different energy windows. The left panels are the results of integration over the ranges (a) (-0.125, 0.125) eV, (c) (-0.2, 0.15) eV, and (e) (-0.35, 0.35) eV. The right panels are the corresponding complementary results of integration up to ± 1 eV with the respective ranges on the left excluded: (b) (-1, -0.125) & (0.125, 1) eV, (d) (-1, -0.2) & (0.15, 1) eV, and (f) (-1, -0.35) & (0.35, 1) eV. Solid red and blue lines are fits to a Gaussian peaks plus an underlying linear *H* dependence (black dashed line).

7. High-temperature CDW fluctuation in $YBa_2Cu_3O_{6+\delta}$ (YBCO)

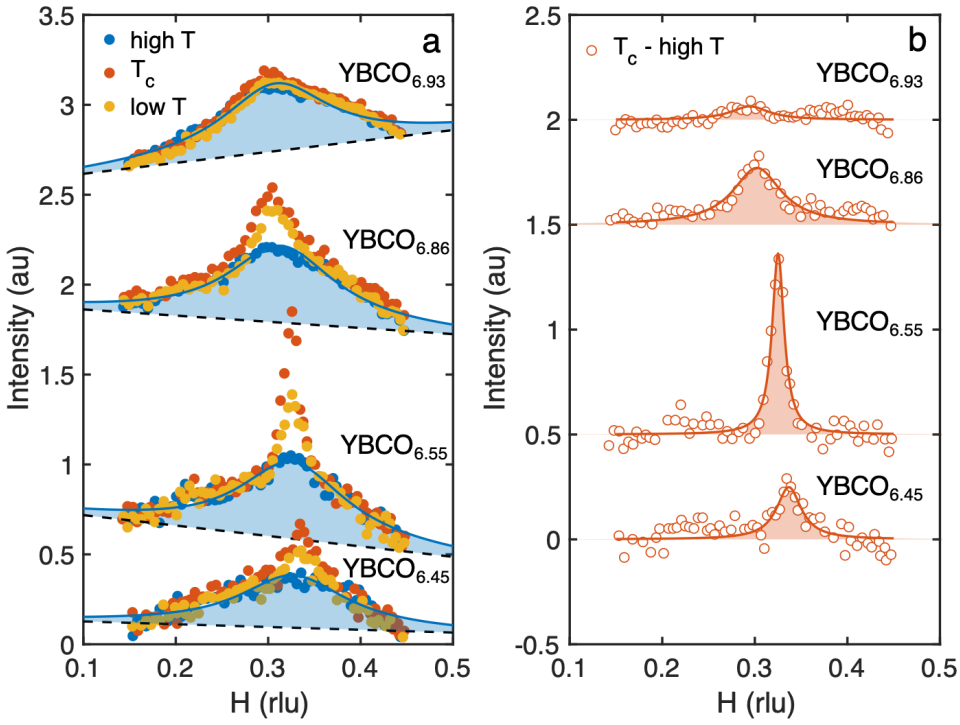


Fig. S10. Evidence for high-temperature charge fluctuations in YBCO measured by RXS. (a) Raw RXS spectra reproduced from [S9]. The broad peaks at high temperature are fit with a Lorentzian profile (solid blue line) on top of linear background (black dashed line). The shaded blue areas indicate the 1D spectral weight of the broad peak. (b) Spectra measured at T_c after subtracting the broad peak in (a). The solid red lines are fits to a narrow Lorentzian peak, associated with quasistatic CDW correlations, and the red shaded areas indicate the 1D spectral weight.

Similar to the data for Hg1201, Bi2201 and NCCO summarized in Fig. 5, the extensively studied cuprate YBCO exhibits a local maximum around $\boldsymbol{q}_{CDW}$ at high temperature. In Fig. S10, we show that the high-temperature YBCO RXS spectra of ref. [S9] are well described by a Lorentzian line shape. The nearly-incoherent high-temperature response is approximately independent of doping in the studied hole concentration range. Long-range CDW order is seen to grow on top of this nearly-incoherent charge scattering at low temperature, and in a relatively narrow doping range. The intensity of the incoherent charge scattering can then be calculated from its 2D spectral weight integrated over the whole Brillouin zone. For $YBCO_{6.55}$ and $YBCO_{6.86}$, the ratio of the 2D spectral weight at high temperature to that at low temperature is about 12, consistent with the recent results for NBCO in ref. [S8]. As discussed in the main text, the large underlying signal is dominated by dynamic charge correlations. One possibility why this signal is not seen in Fig. 5 might be that it is largely incoherent in single-layer cuprates.

[S1] A. Yamamoto, W.-Z. Hu, and S. Tajima, Thermoelectric power and resistivity of $HgBa_2CuO_{4+d}$ over a wide doping range, Phys. Rev. B **63**, 024504 (2000).

[S2] L. Braicovich, J. Van Den Brink, V. Bisogni, M. M. Sala, L. J. P. Ament, N. B. Brookes, G. M. De Luca, M. Salluzzo, T. Schmitt, V. N. Strocov, and G. Ghiringhelli, Magnetic excitations and phase separation in the underdoped $La_{2-x}Sr_xCuO_4$ superconductor measured by resonant inelastic X-Ray scattering, Phys. Rev. Lett. 104, 3 (2010).

[S3] M. Le Tacon, G. Ghiringhelli, J. Chaloupka, M. M. Sala, V. Hinkov, M. W. Haverkort, M. Minola, M. Bakr, K. J. Zhou, S. Blanco-Canosa, C. Monney, Y. T. Song, G. L. Sun, C. T. Lin, G. M. De Luca, M. Salluzzo, G. Khaliullin, T. Schmitt, L. Braicovich, and B. Keimer, Intense paramagnon excitations in a large family of high-temperature superconductors, Nat. Phys. **7**, 725 (2011).

[S4] M. P. M. Dean, G. Dellea, R. S. Springell, F. Yakhou-Harris, K. Kummer, N. B. Brookes, X. Liu, Y.-J. Sun, J. Strle, T. Schmitt, L. Braicovich, G. Ghiringhelli, I. Božović, and J. P. Hill, Persistence of magnetic excitations in $La_{2-x}Sr_xCuO_4$ from the undoped insulator to the heavily overdoped non-superconducting metal, Nat. Mater. **12**, 1019 (2013).

[S5] R. Coldea, S. M. Hayden, G. Aeppli, T. G. Perring, C. D. Frost, T. E. Mason, S. W. Cheong, and Z. Fisk, Spin waves and electronic interactions in La2CuO4, Phys. Rev. Lett. **86**, 5377 (2001).

[S6] N. S. Headings, S. M. Hayden, R. Coldea, and T. G. Perring, Anomalous high-energy spin excitations in the high-Tcsuperconductor-parent antiferromagnet La2CuO4, Phys. Rev. Lett. **105**, 247001 (2010).

[S7] Y. Murakami and S. Ishihara, Resonant X-Ray Scattering in Correlated Systems (Springer Tracts in Modern Physics, 2017).

[S8] R. Arpaia, S. Caprara, R. Fumagalli, G. De Vecchi, Y. Y. Peng, E. Andersson, D. Betto, G. M. De Luca, N. B. Brookes, F. Lombardi, M. Salluzzo, L. Braicovich, C. Di Castro, M. Grilli, and G. Ghiringhelli, Dynamical charge density fluctuations pervading the phase diagram of a Cu-based high-T_c superconductor, Science **365**, 906 (2019).

[S9] S. Blanco-Canosa, A. Frano, E. Schierle, J. Porras, T. Loew, M. Minola, M. Bluschke, E. Weschke, B. Keimer, and M. Le Tacon, Resonant X-ray Scattering Study of Charge Density Wave Correlations in $YBa_2Cu_3O_{6+x}$, Phys. Rev. B **90**, (2014).